

Spin and orbital excitations through the metal-to-insulator transition in $\text{Cd}_2\text{Os}_2\text{O}_7$ probed with high-resolution resonant inelastic x-ray scattering

J. G. Vale^{1,2,*}, S. Calder^{3,†}, N. A. Bogdanov^{4,5}, C. Donnerer¹, M. Moretti Sala^{6,‡}, N. R. Davies⁷, D. Mandrus^{8,9}, J. van den Brink⁴, A. D. Christianson^{3,9,10} and D. F. McMorrow¹

¹London Centre for Nanotechnology, University College London (UCL), Gower Street, London WC1E 6BT, United Kingdom

²Laboratory for Quantum Magnetism, École Polytechnique Fédérale de Lausanne (EPFL) CH-1015, Switzerland

³Neutron Scattering Division, Oak Ridge National Laboratory, Oak Ridge, Tennessee 37831, USA

⁴Institute for Theoretical Solid State Physics, IFW Dresden, D01171 Dresden, Germany

⁵Max Planck Institute for Solid State Research, Heisenbergstraße 1, 70569 Stuttgart, Germany

⁶European Synchrotron Radiation Facility (ESRF), CS 40220, F-38043 Grenoble Cedex, France

⁷Clarendon Laboratory, University of Oxford, Parks Road, Oxford OX1 3PU, United Kingdom

⁸Department of Materials Science and Engineering, University of Tennessee, Knoxville, Tennessee 37996, USA

⁹Materials Science and Technology Division, Oak Ridge National Laboratory, Oak Ridge, Tennessee 37831, USA

¹⁰Department of Physics and Astronomy, University of Tennessee, Knoxville, Tennessee 37996, USA



(Received 14 December 2018; revised manuscript received 7 January 2020; published 27 January 2020)

High-resolution resonant inelastic x-ray scattering measurements ($\Delta E = 46$ meV) have been performed on $\text{Cd}_2\text{Os}_2\text{O}_7$ through the metal-to-insulator transition (MIT). A magnetic excitation at 125 meV evolves continuously through the MIT, in agreement with recent Raman-scattering results, and provides further confirmation for an all-in all-out magnetic ground state. Asymmetry of this feature is likely a result of coupling between the electronic and the magnetic degrees of freedom. We also observe a broad continuum of interband excitations centered at 0.3 eV energy loss. This is indicative of significant hybridization between Os 5d and O 2p states and the concurrent itinerant nature of the system. In turn, this suggests a possible breakdown of the free-ion model for $\text{Cd}_2\text{Os}_2\text{O}_7$.

DOI: [10.1103/PhysRevB.101.014441](https://doi.org/10.1103/PhysRevB.101.014441)

I. INTRODUCTION

A number of osmates undergo unconventional metal-to-insulator transitions (MITs) which appear to be driven to some degree by the onset of antiferromagnetic order, notably NaOsO_3 and $\text{Cd}_2\text{Os}_2\text{O}_7$. The former has been proposed to be a rare example of a Slater insulator in three dimensions [1–7], albeit with some controversy [8]. Like NaOsO_3 , bulk measurements on $\text{Cd}_2\text{Os}_2\text{O}_7$ show a direct correspondence between the MIT and the onset of antiferromagnetism at $T_N = 227$ K [9–12]. Resistivity data indicate that a BCS-like indirect charge gap ($2\Delta_C = 80$ meV) opens continuously below the MIT [10,12]. Optical conductivity measurements reveal similar behavior for the direct optical gap ($2\Delta_O = 158$ meV) [13,14] with the most recent study suggesting a weak decoupling of the two phenomena [14]. This manifests as the formation of an apparent antiferromagnetic metallic phase between 210 K and T_N [15]. These observations, along with density functional theory (DFT) calculations [16] led to the suggestion that $\text{Cd}_2\text{Os}_2\text{O}_7$ undergoes a Lifshitz transition

(change in topology of the Fermi surface), which is partly driven by the onset of antiferromagnetic order.

Yet there have been comparatively few studies of the magnetic behavior of $\text{Cd}_2\text{Os}_2\text{O}_7$. Yamaura *et al.* proposed an all-in all-out (AIAO) $\mathbf{k} = 0$ magnetic structure for $\text{Cd}_2\text{Os}_2\text{O}_7$, based upon resonant elastic x-ray scattering data and representation analysis [11]. This was confirmed by the authors of the present article using neutron powder diffraction [17]. Such a ground state has also been unambiguously found for the isostructural $R_2\text{Ir}_2\text{O}_7$ ($R = \text{Sm}, \text{Nd}$) [18,19] and is a direct manifestation of the significant spin-orbit coupling (SOC) present in these systems. Recent measurements have shown that the Néel temperature T_N is continuously suppressed as a function of applied hydrostatic pressure, going to zero temperature at 36 GPa [20]. Such behavior is consistent with the expectations for a Lifshitz transition and its underlying $T = 0$ quantum critical point.

The effect of SOC also extends to the magnetic excitations. Previous low-resolution ($\Delta E = 130$ meV) resonant inelastic x-ray scattering (RIXS) results presented a dispersionless feature in the excitation spectra for $\text{Cd}_2\text{Os}_2\text{O}_7$ at 170 meV, which could not be explained in terms of intra- t_{2g} spin-flip excitations or a simple spin-wave picture [17]. Quantum chemistry (QC) calculations using a nearest-neighbor Heisenberg Hamiltonian [21], which included significant single-ion anisotropy (SIA) and the Dzyaloshinskii-Moriya (DM)

*j.vale@ucl.ac.uk

†caldersa@ornl.gov

‡Present address: Department of Physics, Politecnico di Milano, Piazza Leonardo da Vinci 32, 20133 Milano, Italy.

interaction,

$$\mathcal{H} = J \sum_{ij} \mathbf{S}_i \cdot \mathbf{S}_j + \mathbf{d} \sum_{ij} \mathbf{S}_i \times \mathbf{S}_j + \sum_i \mathbf{S}_i \cdot \mathbf{A} \cdot \mathbf{S}_i \quad (1)$$

had determined the antiferromagnetic exchange parameter $J = 6.3$ meV, considerably smaller than the energy scale of the new peak. Based on exact diagonalization (ED) calculations using the same Hamiltonian, it was concluded that the new feature (henceforth referred to as peak A) was a signature of a combination of $\Delta S = 1$ –3 excitations: $S_z = 3/2 \rightarrow 1/2$ ($\Delta S_z = 1$), $S_z = 3/2 \rightarrow -1/2$ ($\Delta S_z = 2$), and $S_z = 3/2 \rightarrow -3/2$ ($\Delta S_z = 3$). The latter of these was found to be the dominant process in the density of states (DOS) and previously unobserved by RIXS [22]. Excitations with $\Delta S = 3$ are usually forbidden in the RIXS process; however, it was argued that, due to strong spin-orbit coupling in the intermediate state, S was no longer a good quantum number. Hence, the excited-state wave function is composed of a superposition of different spin-orbital states, all of which have a finite overlap with the $S = 3/2$ ground state. Recent Raman-scattering measurements, meanwhile, reveal two broad features at 130 and 150 meV [23], proposed to arise from $\Delta S = 0$ scattering from the two-magnon density of states. It was found that the coupling parameters were generally in good agreement with the previous QC calculations [21].

In this paper, we present high-resolution RIXS measurements ($\Delta E = 46$ meV) on $\text{Cd}_2\text{Os}_2\text{O}_7$. Our results provide new information about the electronic and magnetic excitations in this material as a function of momentum transfer. We determine that the magnetic feature (peak A) has a lower energy than previously reported (125 meV) but has minimal dispersion within experimental uncertainty. By modeling the magnetic excitations well below T_N , we confirm that peak A includes higher-order processes in ΔS and unambiguously establish that the magnetic ground state is AIAO. At higher temperatures, the excitation becomes progressively more damped, potentially abating above the MIT. Notably an asymmetry can be observed at all temperatures, which was previously unresolved in the low-resolution RIXS measurements. It is proposed that this results from coupling between the electronic and the magnetic degrees of freedom, further highlighting the interplay of these phenomena in this system. We also find that the orbital excitations exhibit a degree of $5d^4$ character, despite the nominal electronic ground state being $5d^3$. This is likely due to significant hybridization and long-ranged electronic interactions, which go beyond a simple free-ion model for $\text{Cd}_2\text{Os}_2\text{O}_7$.

II. EXPERIMENTAL DETAILS

RIXS measurements at the Os L_3 edge (10.871 keV) were performed on a single crystal of $\text{Cd}_2\text{Os}_2\text{O}_7$ (~ 0.5 mm across) on the ID20 spectrometer at the ESRF, Grenoble [24]. The sample was oriented such that the $[1, 1, 1]$ direction was perpendicular to a copper sample mount, fixed with GE varnish, and placed in a closed-flow (Dynaflow) He cryostat. The scattering plane and incident photon polarization were both horizontal, i.e., π -incident polarization with the incident beam focused to a size of $20 \times 10 \mu\text{m}^2$ ($H \times V$) at the sample position.

A Si (6, 6, 4) four-bounce secondary monochromator was used to define the incident energy, with a Si (6, 6, 4) diced spherical analyzer (2 m radius, 40 mm diameter mask) used to reflect the scattered photons towards a Medipix CCD detector (pixel size $55 \mu\text{m}$). Total energy resolution was determined to be $\Delta E = 46$ meV based on scattering from a structural Bragg reflection.

III. LOW-TEMPERATURE BEHAVIOR

We first examine the low-energy behavior deep in the antiferromagnetic insulating phase (30 K). This permits detailed study of the spin Hamiltonian towards the localized limit.

A. RIXS

RIXS spectra collected in the (6, 7, 7) Brillouin zone are plotted in Fig. 1(a) as a function of momentum transfer. At first glance, they appear similar to those presented in Ref. [17]. The main distinction, however, is that peak A exhibits a degree of asymmetry not observed in the previous study. In order to quantify our observations further, the data were modeled with Gaussians to represent the elastic line and high-energy intra- t_{2g} excitations. A suitable line shape was added to describe the asymmetric magnetic feature (peak A), and the resultant function was convoluted with the experimental resolution function prior to fitting. A number of models was considered which take this asymmetry into account with the best found to be a Breit-Wigner-Fano peak shape, given by

$$I(\omega) = I_0 \frac{[1 + (\omega - \omega_0)/q\Gamma]^2}{1 + [(\omega - \omega_0)/\Gamma]^2}. \quad (2)$$

Such a model successfully described the effect of spin-phonon coupling observed in Raman scattering [23,25]. The asymmetry is a direct manifestation of coupling between a resonant mode (with lifetime $\propto 1/\Gamma$, where Γ is a damping parameter) and a continuum of states, the magnitude of which is parametrized by the coefficient $|1/q|$. Note that, in the subsequent analysis, it has been assumed that $q \approx 7$ —indicative of moderate coupling between the resonance and the continuum—is globally fixed for all temperatures and momentum transfers. This is due to insufficient data between the peak maximum and the broad elastic line. In this region, the functional form of the line shape is especially sensitive to the magnitude of q . It was found that the quality of the fit was consistently improved at all temperatures and momentum transfers by the inclusion of a broad weakly dispersive feature centered at approximately 300 meV [Fig. 1(d)]. This feature—henceforth referred to as peak A2—was assumed to have a Gaussian line shape; potential origins are discussed later.

The energy and spectral weight of peak A are plotted in Figs. 1(b) and 1(c). Within experimental uncertainty, peak A exhibits minimal dispersion throughout the Brillouin zone with little concurrent weak variation in the spectral weight. Using the AIAO magnetic ground state and Eq. (1) as a starting point, we were able to successfully model the observed behavior within linear spin-wave theory (LSWT). This implies that this minimal Hamiltonian is sufficient to describe the magnetic interactions in $\text{Cd}_2\text{Os}_2\text{O}_7$. The coupling parameters we extract, however, are a factor of 2 larger than

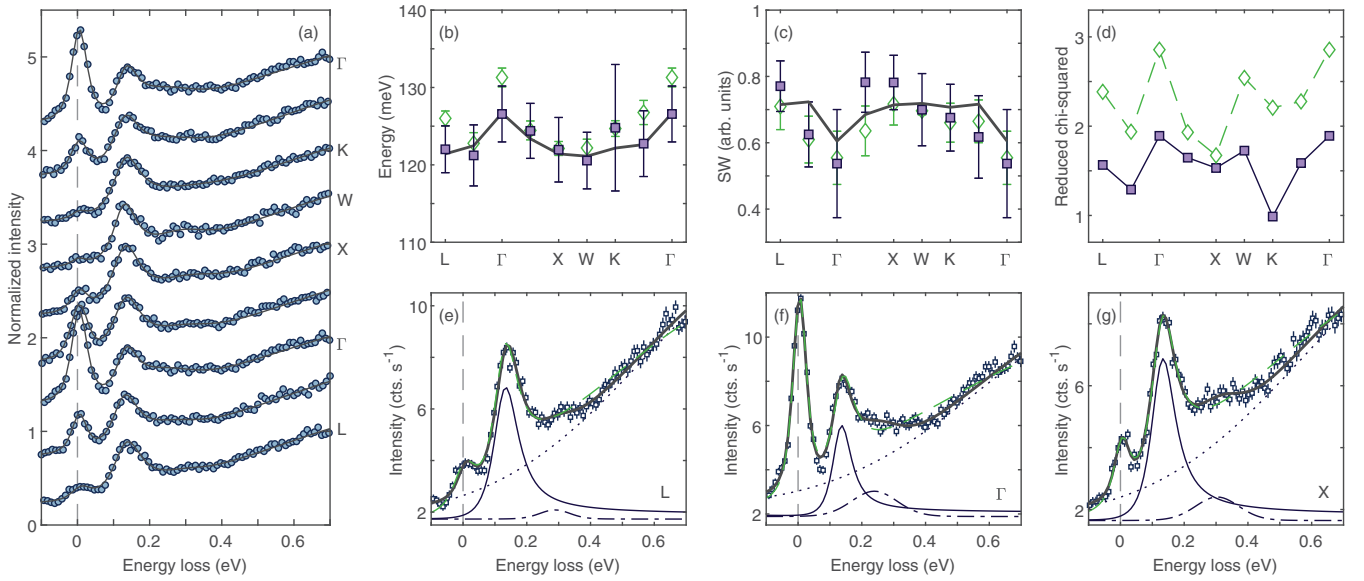


FIG. 1. (a) RIXS spectra as a function of momentum transfer collected in the (6, 7, 7) Brillouin zone at 30 K. Spectra are normalized to the d - d excitations at 0.7 eV and offset for clarity. The black solid lines are the best fit to the model described in main text (including a feature at 0.3 eV). (b)–(d) Extracted fitting parameters with(out) broad features at 0.3 eV given by the filled squares (the open diamonds). The energy and spectral weight of peak A are plotted in (b) and (c) with the corresponding reduced χ^2 of the fits given in (d). The solid lines in (b) and (c) are best fit to Hamiltonian given by Eq. (1) with parameters $J = 13.1$, $A = -12.9$, and $|d| = 6.8$ meV. (e)–(g) Comparison of the fits at different momentum transfers. The solid and dot-dashed peaks represent Fano resonance and 0.3 eV feature components, respectively. The dashed green line indicates the fit without the 0.3 eV feature.

determined from quantum chemistry calculations and Raman scattering (Table I). This discrepancy is rather puzzling, and we considered alternative explanations.

B. Verification of the magnetic ground state and Hamiltonian

We first ascertained how the magnitude of different coupling parameters influence the magnetic ground state and, hence, the validity of the putative magnetic Hamiltonian. An isotropic Heisenberg antiferromagnet on the pyrochlore lattice exhibits geometric frustration. Due to the lattice topology, it is not possible to simultaneously satisfy all of the pairwise interactions between spins. Consequently, no long-ranged order is observed down to $T \rightarrow 0$ with the resulting ground state being highly degenerate. Introducing anisotropy (or further neighbor interactions) breaks this degeneracy, leading to a unique magnetic ground state. In the case of zero SIA, the magnetic ground state depends on the sign of the DM vector. If the DM vector is negative (direct DM interaction), then one obtains the AIAO arrangement of spins (irreducible representation Γ_3). This situation exactly corresponds to that

determined for $R_2\text{Ir}_2\text{O}_7$ [18]. Meanwhile, if the DM vector is positive (indirect DM interaction), then the spins are confined to the xy plane (Γ_5). Adding uniaxial SIA along the local $\langle 111 \rangle$ direction (compressive trigonal distortion of the OsO_6 octahedra) actually helps to stabilize the AIAO ground state. Bogdanov *et al.* argue that this is the dominant driving force for putative AIAO order in $\text{Cd}_2\text{Os}_2\text{O}_7$ with the DM interaction playing a more minor role [21].

The results of a semiclassical energy minimization of a Heisenberg antiferromagnet on the pyrochlore lattice are plotted in Fig. 2(e) for different values of SIA and the DM interaction. Note that negative SIA corresponds to a uniaxial anisotropy along the local $\langle 111 \rangle$ direction for each moment. We find that the resulting ground-state spin configuration is highly dependent upon the choice of coupling parameters with four different ground states occurring in different regions of the phase diagram. These states correspond to the possible magnetic representations $\Gamma_{\text{mag}} = \Gamma_3 + \Gamma_5 + \Gamma_7 + 2\Gamma_9$ for $\mathbf{k} = 0$ order on the pyrochlore lattice. It is possible to go further and calculate the expected spin-wave dispersion for a given set of coupling parameters and magnetic structure. In Figs. 2(a)–2(d), we plot the results of least-squares fits to the experimental dispersion and intensity, which were performed in SPINW [26]. It is clear that an AIAO spin configuration (Γ_3) provides a much better description of the data for sensible values of the coupling parameters.

Further support for an AIAO ground state can be garnered from results of simulated annealing runs. These were performed on system sizes of $L \times L \times L$ unit cells, where L ranges from 1 to 5 (16–2000 spins in total). The energy of the system and its interactions were determined via the Hamiltonian given by Eq. (1). Coupling parameters used were

TABLE I. Comparison of exchange parameters between different studies, given in units of meV.

	J	$ d $	A	$J/ d $	J/A
DFT ($U_{\text{eff}} = 1.25$ eV) [16]	14	4	-24	3.5	-0.6
Quantum chemistry [21]	6.43	1.65	-6.77	3.9	-1.0
Raman [23] (from two magnon)	5.1	1.7	-5.3	3.0	-1.0
RIXS (from raw data)	13.1	6.8	-12.9	1.9	-1.0
RIXS (effective $\Delta S = 1$)	6.5	3.4	-6.5	1.9	-1.0

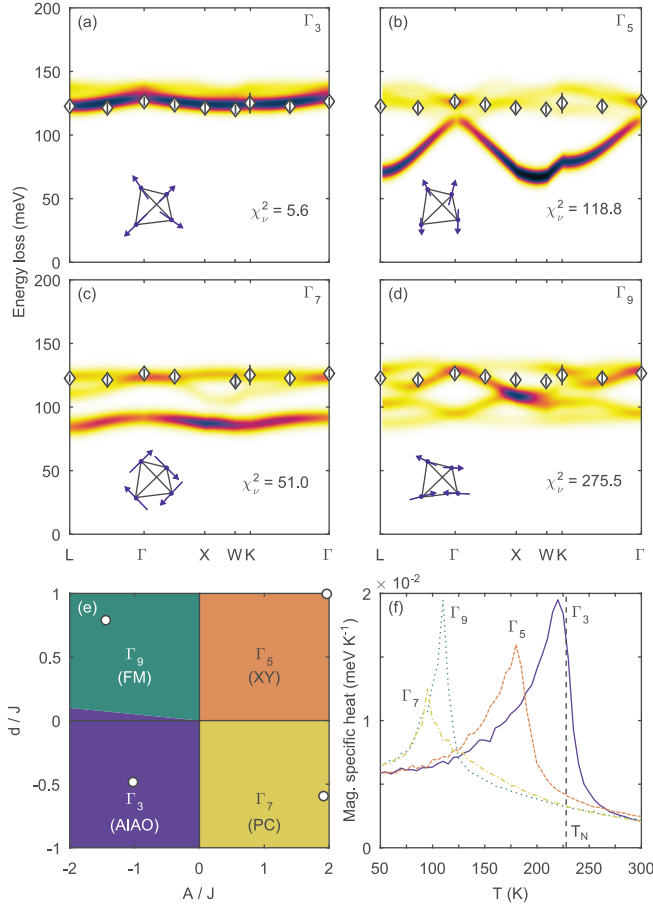


FIG. 2. (a)–(d) Best fits to the experimental dispersion (the open symbols) for different starting magnetic representations Γ_i . Γ_3 : AIO. Γ_5 : XY. Γ_7 : Palmer-Chalker (PC) phase. Γ_9 : ferromagnet (FM). All figures use the same color scale. (e) Phase diagram reflecting the magnetic ground state for different values of the single-ion anisotropy A and the DM vector $\mathbf{d} = (d, d, 0)$. (f) Magnetic specific heat per moment obtained from simulated annealing [$L = 3$, $J = 13.1(3)$ meV]. The open symbols in (e) indicate the parameters which were used for the remaining figures.

the same as those obtained from the fits to the spin-wave dispersion in Figs. 2(a)–2(d), albeit divided by 2 [27]. The simulated annealing was performed with a standard Metropolis spin-flip algorithm with 5×10^4 Monte Carlo steps (MCSs) per spin to equilibrate the system for a given temperature, followed by a further 5×10^4 MCSs per spin to evaluate thermodynamic parameters. Two sets of runs were performed for each system size: one with a relatively coarse temperature step ($T_{\text{new}} = 0.92T$) initialized at 2000 K ($T/J \approx 25$) with the spins oriented randomly and a dataset focusing on the critical region. The latter was initialized at 320 K (experimentally $T_N + 93$ K) with the state obtained from the coarse dataset at the same temperature and run with a step size of 5 K.

The results of these simulations are plotted in Fig. 2(f) for $L = 3$. In each case, the final ground state was the same as that obtained from the semiclassical energy minimization. As expected, the magnetic specific-heat C_m diverges at the Néel temperature, consistent with a second-order phase transition. For Γ_3 , we find remarkable agreement between the maximum

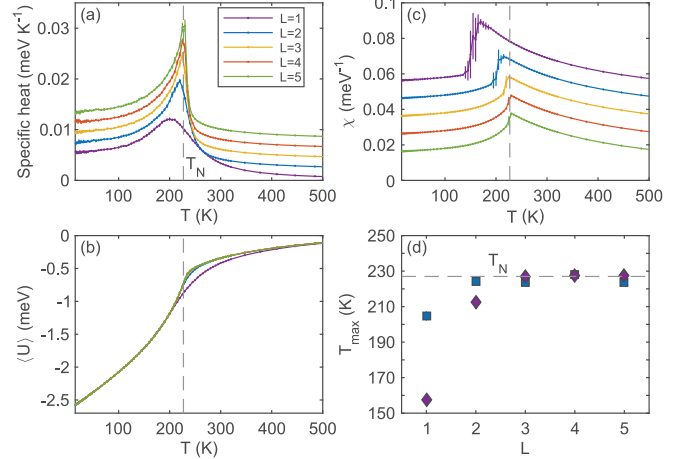


FIG. 3. Results from simulated annealing runs performed for different system sizes of $\text{Cd}_2\text{Os}_2\text{O}_7$. All data displayed occur from the mean of five successive runs with error bars reflecting the standard deviation about this mean. Parameters plotted (per magnetic moment) are the (a) magnetic specific-heat C , (b) isothermal susceptibility χ , and (c) mean internal energy $\langle U \rangle$. The curves in (a) and (c) have been offset for clarity. In (d), the fitted maximum of the specific heat (squares) and susceptibility (diamonds) has been plotted. The dashed lines indicate the experimental Néel temperature T_N . There appears to be a convergence of the calculated T_N with the experimental one in the thermodynamic limit.

of C_m and the experimental Néel temperature ($T_N = 227$ K). The other magnetic representations, however, appear to significantly underestimate T_N . This suggests that the AIO spin configuration is, indeed, the correct one for $\text{Cd}_2\text{Os}_2\text{O}_7$. We tested this further by examining the effect of the finite-sized lattice upon the thermodynamic properties (Fig. 3). The continuous phase transition observed in the magnetic specific heat and susceptibility appears to sharpen and converge towards the experimental Néel temperature $T_N = 227$ K with increasing system sizes. This would be expected as one progresses towards the thermodynamic limit.

There are, however, a number of limitations with the simulations as presented here. First, there is a fundamental problem in the Metropolis spin-flip algorithm of “critical slowing down.” In the vicinity of the critical point, equilibration is slow as both the length and the timescales involved diverge. Thus, there are frequent problems with accurate determination of transition temperatures and critical exponents within this approach. Improvements could be made by utilizing a cluster-flipping algorithm where critical slowing down is dramatically reduced. Second, the number of equilibration and averaging steps per spin is relatively low. Ideally, one would want to perform the simulations with a greater number of steps to ensure equilibration and accurately determine the thermodynamic parameters with appropriate statistical error bars. The number of MCSs performed per spin was sufficient to ensure equilibration for each temperature and lattice size, however, as determined from the temporal dependence of the internal energy. Sharp fluctuations can also be observed in the internal energy (U) and magnetization at low temperature ($T < 20$ K). These fluctuations occur over a single temperature step

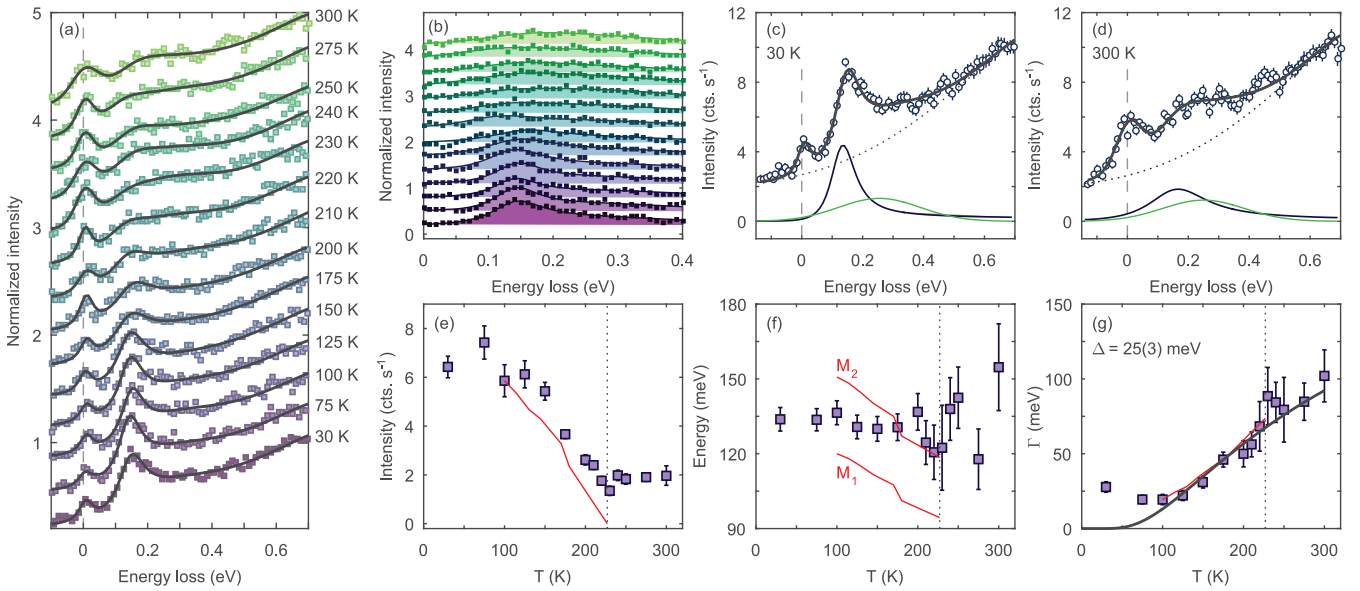


FIG. 4. Temperature dependence of RIXS spectra collected at (7, 7, 8). (a) Stack plot of data normalized to intensity of intra- t_{2g} excitations at 0.7 eV, plotted with best fit to the data. (b) Normalized data with elastic and intra- t_{2g} contributions subtracted. There is a clear evolution of the line shape from 30 K (bottom) to 300 K (top) as the gap closes. (c) and (d) Fits at (c) 30 K and (d) 300 K. (e)–(g) (e) Temperature dependence of intensity, (f) uncoupled resonance energy ω_0 , and (g) damping parameter Γ . The red solid lines are data extracted from Raman-scattering measurements [23], which are normalized to 100 K values in (e) and (g). The black line in (g) is best fit to $\Gamma = A \exp(-\Delta/k_B T)$ below T_{MI} .

and may be due to some long timescale behavior which has been incorrectly compensated for in the averaging procedure. Performing a full autocorrelation analysis is likely to improve this.

Finally, a complete finite-size scaling analysis has not been performed. Transition temperatures determined from the magnetization, for example, for a given lattice size frequently do not represent the true behavior of the system in the thermodynamic limit. This is why the maxima of the magnetic specific-heat and susceptibility curves have been plotted in Fig. 3(d) instead of the calculated Néel temperature. Practically what one would do within a finite-size scaling analysis is to calculate the Binder cumulant for each temperature and lattice size and determine their crossing point via a data collapse. Such an analysis is somewhat subjective, however, since it requires some fine-tuning of the critical temperature and critical exponents to obtain the correct crossing point.

Despite these limitations, the simulations appear to provide further evidence for an AIAO magnetic ground state in $\text{Cd}_2\text{Os}_2\text{O}_7$. In particular, we obtain remarkable agreement between the calculated and the experimental Néel temperatures for a set of coupling parameters (divided by 2 relative to the values obtained experimentally) that best fits the observed spin-wave dispersion. This validates the choice of Hamiltonian, although the factor of 2 discrepancy with the RIXS results remains puzzling.

IV. TEMPERATURE DEPENDENCE

Now, that the low-energy excitations have been characterized deep in the antiferromagnetic insulating phase, we establish how they vary through the MIT. RIXS spectra were collected at the (7, 7, 8) Brillouin-zone center Γ as a function of temperature. Note that this is in a different Brillouin

zone from the momentum dependence data presented in the previous section; the advantage is that the quasielastic peak is noticeably suppressed due to the scattering angle 2θ being closer to the ideal condition of $2\theta = 90^\circ$.

The results are shown in Fig. 4. Utilizing the same fitting model as used previously, we observe a clear evolution of the line shape of peak A from 30 to 300 K [Figs. 4(b)–4(d)]. The intensity of this peak decreases continuously as a function of increasing temperature, abating at ~ 230 K [Fig. 4(e)]. This coincides with the Néel temperature and is consistent with the previous RIXS and Raman-scattering results [17,23]. Meanwhile, the peak energy appears approximately constant through the MIT (within experimental resolution) [Fig. 4(f)]. This contrasts with the Raman-scattering data, which show that the two-magnon peaks M_1 and M_2 are weakly renormalized with temperature. Even so, the general energy scale is consistent.

Finally, the magnitude of the damping parameter Γ is approximately resolution limited at low temperatures and increases rapidly above 150 K [Fig. 4(g)]. Note that it is unclear within experimental uncertainty whether Γ saturates above the MIT or simply increases monotonically [28]. There are two possible origins for the observed behavior. The first is that the magnetic excitations become Landau damped by intraband particle-hole excitations. At $T = 0$, optical conductivity measurements have determined the optical gap $2\Delta_O = 158$ meV [14]. The magnitude of $2\Delta_O$ decreases continuously with increasing temperature and becomes comparable to the energy of the magnetic excitations at ~ 150 K. Hence, one would expect the damping to increase accordingly above this temperature. This scenario is broadly consistent with the data. An alternative proposition is that the damping is driven by spin-phonon coupling as already observed by Raman-scattering [23] and optical spectroscopy measurements [25].

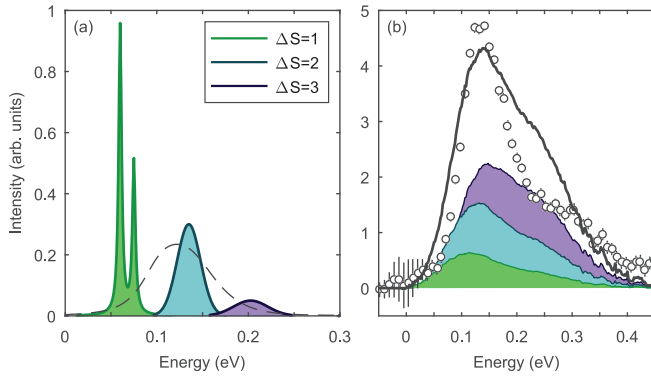


FIG. 5. Schematic of (a) expected magnetic density of states within linear spin-wave theory, and (b) that determined within exact diagonalization. The dashed line in (a) represents the effect of mixing between ΔS modes. The data points plotted in (b) are the sum of all the data presented in Fig. 1(a) with elastic and $d-d$ contributions subtracted off. This is a crude approximation of the RIXS density of states determined from ED.

From fitting the data above 100 K to an Arrhenius function: $\Gamma = A \exp(-\Delta/k_B T)$, we find that the critical energy scale is $\Delta = 25(3)$ meV. This is in good agreement with the lowest-energy Os phonon modes, both infrared active [Os-Os stretch, 24.6(5) meV] and Raman active [Os-O(1) stretch, 28 meV]. At present, it is not possible to disentangle these two pictures.

V. DISCUSSION

Thus far, we have determined that the magnetic excitations in $\text{Cd}_2\text{Os}_2\text{O}_7$ are indicative of coupling between a number of different degrees of freedom. Furthermore, we have unambiguously confirmed the AIAO magnetic ground state and relevant leading-order terms in the Hamiltonian. There are, however, some outstanding questions. Raman-scattering measurements, quantum chemistry calculations, and classical Monte Carlo simulations have all obtained values of the exchange parameters which broadly agree with one another (Table I). Yet the momentum dependence of the feature observed by RIXS appears to be best described by a Hamiltonian dictated by significantly larger coupling parameters ($J = 13.1$ meV, $|d| = 6.8$ meV, $A = -12.9$ meV). We suggest a possible origin for this discrepancy. In the semiclassical limit (LSWT) and assuming no magnon damping, one would expect magnon branches ($\Delta S = 1$) at 65 and 75 meV and a two-magnon ($\Delta S = 0, 2$) continuum between 130 and 150 meV. The kinematic $\Delta S = 3$ continuum would be between 195 and 225 meV [Fig. 5(a)]. If mixing occurs between these different ΔS terms, then presumably they would move closer together in energy. The corresponding peak in the imaginary part of the dynamic susceptibility $\chi''(\mathbf{Q}, \omega)$ would, consequently, be shifted towards the nominal $\Delta S = 2$ value. We show this heuristic picture by the dashed line in Fig. 5(a). Such a scenario would qualitatively agree with the results of the ED calculations as presented in Ref. [17], which equate to the quantum limit.

Even so, the ED calculations cannot fully describe all of the details observed in the experimental data. In order to better compare with theory, all of the data presented in Fig. 1(a) have been summed together, and the respective elastic and $d-d$

components subtracted off. This acts as a crude approximation for the magnetic part of the RIXS DOS. We compare this in Fig. 5(b) with the theoretical RIXS intensity calculated by ED, which is shown *without* the effect of instrumental broadening. Although the energy scale of the excitations agree, there are discrepancies in the line shape between experiment and theory especially above 200 meV.

There are a number of factors which are likely to contribute. First, the intensity observed experimentally actually corresponds to the RIXS scattering cross section, which is significantly more difficult to calculate than the RIXS DOS. It is likely that the RIXS cross section will be dominated by the $\Delta S = 1$ component as opposed to $\Delta S = 3$. Fano coupling will also remove spectral weight at low energies and shift it to higher energies. Finally, the ED calculations used coupling parameters determined from quantum chemistry calculations [21]; Nguyen *et al.* have already shown that the experimental values obtained from Raman scattering appear to be slightly lower [23].

Recall that the fit to the data was significantly improved at all temperatures and momentum transfers upon the inclusion of a broad weakly dispersive feature (peak A2) centered at 0.3 eV energy loss [Fig. 1(d)]. No significant temperature dependence was observed [Figs. 4(c) and 4(d)], which implies that it is likely to have an electronic, rather than a magnetic, origin. A similar feature observed in NaOsO_3 was suggested to result from interband transitions based on calculations of the electronic band structure from DFT [29]. We performed a similar analysis for $\text{Cd}_2\text{Os}_2\text{O}_7$ using the previously published results by Shinaoka *et al.* calculated in the local spin-density approximation [16], including spin-orbit coupling and on-site Coulomb repulsion U (LSDA + SO + U) [Fig. 6(a)]. The effective coupling $U_{\text{eff}} = U - J$ was taken to be 1.25 eV, which the authors of Ref. [16] found gave a ground state which was close to the MIT but still in the antiferromagnetic insulating phase. For simplicity, the two electronic bands closest to the Fermi level were fitted in the parabolic approximation using the band energies at high-symmetry points to constrain the fits and assuming that the band minimum is at Γ . The results are shown in Fig. 6(b) with all the main features of the two electronic bands reasonably reproduced.

Dipole-allowed interband transitions were calculated using a Monte Carlo approach. Two wave vectors in the Brillouin zone were randomly selected; these correspond to states in the valence and conduction bands which each have some particular energy. The difference in energy and wave vector between these states was computed and mapped back onto the first Brillouin zone. This was repeated 4×10^8 times with the result shown in Fig. 6(c). A broad feature can be seen in the data which are centered around 0.55 eV. Along the Γ -L and Γ -X directions, however, a continuum of states can be clearly seen which extends to lower energies. Comparing the results at Γ with experimental data taken at 200 K [Fig. 6(d)], we find a weak peak at 0.6 eV which is consistent with the energy scale of our excitations. Moreover, the low-energy continuum appears to be centered at around 0.25 eV. This suggests that the broad continuum observed previously [Fig. 4(d)] does, indeed, manifest from interband transitions.

It should be noted that our conclusions come with a number of limitations. First, our calculations only considered the two

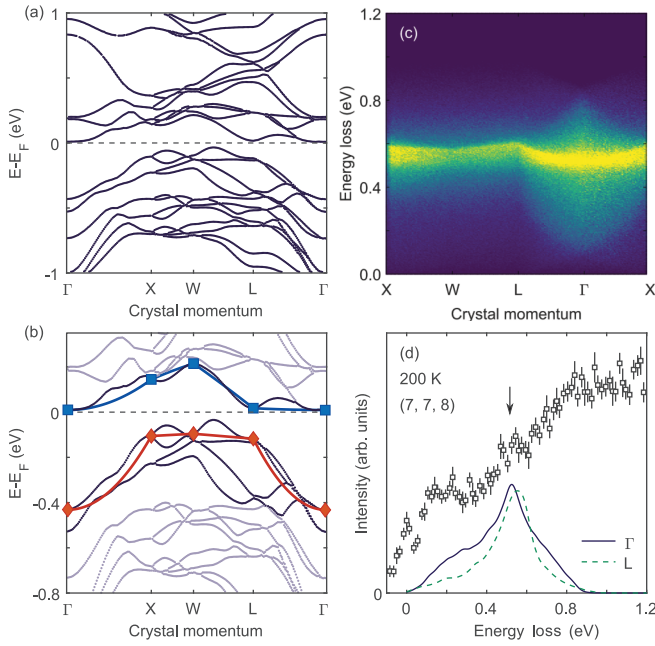


FIG. 6. (a) Electronic band structure of $\text{Cd}_2\text{Os}_2\text{O}_7$ close to the Fermi-level E_F , calculated using density functional theory for $U_{\text{eff}} = 1.25$ eV [16]. (b) Bands close to E_F , along with the best fit in the parabolic band approximation. (c) Calculation of dipole-allowed interband transitions between bands close to E_F , calculated as described in the main text. (d) RIXS spectrum collected at $(7, 7, 8)$ compared with the calculated spectra at Γ and L . The effect of the instrumental resolution has been included. The arrow highlights a weak feature at 0.6 eV.

closest bands to the Fermi level and assumed they were parabolic. Additional contributions from neighboring bands will modify the line shape somewhat, especially at higher-energy loss [Figs. 6(a) and 6(b)]. The parabolic band approximation also averages over a degree of fine-structure which is clearly present from the DFT calculations. Furthermore, RIXS at the L_3 edge is not a direct probe of the band structure even in weakly correlated systems. Finally, we have neglected likely Q -dependent matrix element effects, which enter the RIXS cross section. This may explain the difference in the fitted width of peak A2 for different Brillouin zones at the same high-symmetry point [Figs. 1(f) and 4(c)]. Nevertheless, the presence of interband transitions appears to provide an excellent description of the experimental data.

Our results clearly show the itinerant (nonlocal) nature of $\text{Cd}_2\text{Os}_2\text{O}_7$. Osmium containing transition-metal oxides (TMOs) are typically characterized by significant hybridization between the extended $5d$ orbitals on the osmium site and the $2p$ orbitals on the oxygen sites [30–35]. For instance, in NaOsO_3 , it was determined by DFT that there were, on average, 4.3 d electrons per Os site, instead of the nominal three [4]. Quantum chemistry calculations on a small cluster find that the orbital excitations in $\text{Cd}_2\text{Os}_2\text{O}_7$ are generally better described by an Os $5d^4$ electronic configuration rather than the nominal $5d^3$ (the Appendix). Yet, it has been previously demonstrated that the exchange parameters obtained using $5d^3$ are in excellent agreement with experiment (Table I). The complexity of these calculations means that—by

necessity—they neglect the effect of longer-ranged electronic interactions which may be important. Even so, it highlights that a free-ion description is inadequate for $\text{Cd}_2\text{Os}_2\text{O}_7$.

This is even more apparent when comparing a representative RIXS spectrum of $\text{Cd}_2\text{Os}_2\text{O}_7$ with that for the nominally isoelectronic ($5d^3$) $\text{Ca}_3\text{LiOsO}_6$ [35,36]. This insulating double perovskite consists of isolated, almost ideal OsO_6 octahedra separated by Li cations, and consequently, acts as a good approximation to a free-ion model. This is despite strong hybridization between Os $5d$ and O $2p$ orbitals [35]. Four resolution-limited ($\Delta E = 150$ meV) excitations can be observed for $\text{Ca}_3\text{LiOsO}_6$. This contrasts markedly with the situation for $\text{Cd}_2\text{Os}_2\text{O}_7$ where the features are considerably broader despite the improved resolution ($\Delta E = 46$ meV). Note that for L -edge RIXS—in particular, on $5d$ TMOs—the intrinsic width (in energy) of an arbitrary excitation is essentially proportional to the inverse lifetime of the final state. This contrasts with x-ray absorption spectroscopy in which the spectra are broadened by the core hole in the intermediate state. What we observe experimentally is a convolution of this excitation with the spectrometer resolution function. Clearly, the intrinsic width of these excitations is significantly broader for $\text{Cd}_2\text{Os}_2\text{O}_7$ than the experimental resolution. This is indicative of the final state having a short lifetime. We posit this is due to longer-ranged electronic interactions between neighboring OsO_6 octahedra through the shared oxygen site (absent in $\text{Ca}_3\text{LiOsO}_6$), which, in turn, leads to greater itinerancy.

VI. CONCLUSION

We have presented high-resolution RIXS measurements on $\text{Cd}_2\text{Os}_2\text{O}_7$. Our results highlight the complementary information that RIXS and Raman scattering provide. Raman scattering has superior energy resolution and count rates, however, it is only sensitive to zone-center $\Delta S = 0$ excitations as a consequence of selection rules. Meanwhile, RIXS is a momentum-resolved orbital, and element-specific technique, which can probe $\Delta S \neq 0$ excitations due to spin-orbit coupling in the intermediate state. We conclude that the magnetic excitations previously observed by RIXS and Raman scattering essentially correspond to different parts of the same feature. The asymmetry of peak A is proposed to result from coupling between a resonant magnetic process and interband electronic excitations. This further highlights the interplay between the magnetism and the electronic behavior of $\text{Cd}_2\text{Os}_2\text{O}_7$. Moreover, the presence of interband transitions is due to significant hybridization and itinerant behavior and is indicative of a breakdown of the free-ion model frequently used to describe RIXS spectra. This would have ramifications for the analysis of orbital excitations in other systems proximate to a metal-insulator transition and ties in with the description of magnetic excitations in the itinerant and localized regimes [29].

ACKNOWLEDGMENTS

Research in London was supported by the Engineering and Physical Sciences Research Council (Grants No. EP/N027671/1 and No. EP/N034872/1). Work at ORNL's High Flux Isotope Reactor was supported by the Scientific User Facilities Division, Office of Basic Energy Sciences,

U.S. Department of Energy (DOE). J.G.V. would like to thank University College London (UCL) and École Polytechnique Fédérale de Lausanne (EPFL) for financial support through a UCL Impact award. A.D.C. and D.M. acknowledges support from the U.S. Department of Energy, Office of Science – Basic Energy Sciences (BES), Materials Sciences and Engineering Division.

APPENDIX: QUANTUM CHEMISTRY CALCULATIONS

New quantum chemistry calculations were performed for $\text{Cd}_2\text{Os}_2\text{O}_7$ following the protocol described in Ref. [21] for calculating the intrasite excitation energies [37–41]. These calculations simulate the effect of adding one extra electron to the finite cluster, giving rise to a $5d^4$ electronic configuration. The embedded cluster consists of one reference OsO_6 octahedron, six adjacent Cd sites, and six nearest-neighbor OsO_6 octahedra in which Os^{5+} was represented by closed-shell $\text{Ta}^{5+} d^0$ species. The farther environment was modeled as a one-electron effective potential, which, in an ionic picture, reproduces the Madelung field in the cluster region. We performed complete active space self-consistent-field (CASSCF) calculations with four electrons in five orbitals averaging over the lowest six singlet, ten triplet, and two quintet states. In the following multireference configuration interaction (MRCI) computation, we included, on top of the CASSCF wave

TABLE II. MRCI and MRCI + SOC relative energies (eV) for the $\text{Os } 5d^4$ multiplet structure in $\text{Cd}_2\text{Os}_2\text{O}_7$, given to two decimal places. The lowest 18 MRCI + SOC states are shown for brevity. Note that the dominant configuration label only corresponds to the states computed using MRCI.

Dominant configuration	MRCI	MRCI + SOC
$S = 1 \ t_{2g}^4$	0; 0.19; 0.20	0; 0.36; 0.36;
$S = 0 \ t_{2g}^4$	1.10; 1.10; 1.29;	0.52; 0.76; 0.78;
	1.30; 1.32; 2.48	0.78; 0.80; 0.81;
$S = 2 \ t_{2g}^3 e_g^1$	2.77; 2.78	1.74; 1.74; 1.89;
$S = 1 \ t_{2g}^3 e_g^1$	4.14; 4.15; 4.51;	1.94; 1.97; 3.19;
	4.52; 4.52; 4.66;	3.37; 3.39; 3.40...
	4.68	

TABLE III. MRCI and MRCI + SOC relative energies (eV) for the $\text{Os}^{5+} 5d^3$ multiplet structure in $\text{Cd}_2\text{Os}_2\text{O}_7$. Since cubic symmetry is lifted, the T states are split even without SOC. Each MRCI + SOC value stands for a spin-orbit doublet; for the 4T states, only the lowest and highest components are given. Reproduced from Ref. [21].

$5d^3$ splittings	MRCI	MRCI + SOC
$^4A_2 (t_{2g}^3)$	0.00;	0.000; 13.5×10^{-3}
$^2E (t_{2g}^3)$	1.51; 1.51	1.40; 1.53
$^2T_1 (t_{2g}^3)$	1.61; 1.62; 1.62	1.63; 1.66; 1.76
$^2T_2 (t_{2g}^3)$	2.46; 2.49; 2.49	2.63; 2.76; 2.87
$^4T_2 (t_{2g}^2 e_g)$	5.08; 5.20; 5.20	5.14; ...; 5.45
$^4T_1 (t_{2g}^2 e_g)$	5.89; 6.01; 6.01	6.02; ...; 6.33
$^4T_1 (t_{2g}^2 e_g^2)$	10.29; 10.63; 10.63	10.41; ...; 11.00

functions, all single and double excitations from the $\text{Os } 5d$ and $\text{O } 2p$ orbitals at the central octahedron. Finally, the SOC Hamiltonian [42] between all spin components of the 18 spin-free MRCI states is computed and diagonalized resulting in 46 SO states. The splittings between the lowest 18 states are listed in Table II.

We compared the results of these calculations (and those presented in Ref. [21], which are reproduced in Table III) with the experimental data. We find that the agreement with experiment is generally better for a $5d^4$ configuration than for a $5d^3$ configuration. There are two main observations which lead to this conclusion. For instance, previous high-resolution RIXS measurements show broad excitations centered at 4.5 eV (peak B). This was proposed by the authors to result from multiple overlapping $t_{2g}^3 \rightarrow t_{2g}^2 e_g$ transitions [17]. Yet the previous QC calculations (Table III) determine the lowest-energy $t_{2g}^2 e_g$ multiplet to be at 5.1 eV. This overestimate of the energy scales consistently occurs both within MRCI and within MRCI + SOC. Meanwhile, the energy scale of the $S = 1 \ t_{2g}^4 \rightarrow t_{2g}^3 e_g$ excitations appears to match rather well with the experimental results (Table II). We also note that the MRCI + SOC calculations predict an excitation at 0.36 eV; again comparable to the energy of peak A2. This suggests that the electronic behavior of $\text{Cd}_2\text{Os}_2\text{O}_7$ may, indeed, exhibit some $5d^4$ character.

- [1] Y. G. Shi, Y. F. Guo, S. Yu, M. Arai, A. A. Belik, A. Sato, K. Yamaura, E. Takayama-Muromachi, H. F. Tian, H. X. Yang, J. Q. Li, T. Varga, J. F. Mitchell, and S. Okamoto, Continuous metal-insulator transition of the antiferromagnetic perovskite NaOsO_3 , *Phys. Rev. B* **80**, 161104(R) (2009).
- [2] S. Calder, V. O. Garlea, D. F. McMorrow, M. D. Lumsden, M. B. Stone, J. C. Lang, J.-W. Kim, J. A. Schlueter, Y. G. Shi, K. Yamaura, Y. S. Sun, Y. Tsujimoto, and A. D. Christianson, Magnetically Driven Metal-Insulator Transition in NaOsO_3 , *Phys. Rev. Lett.* **108**, 257209 (2012).
- [3] Y. Du, X. Wan, L. Sheng, J. Dong, and S. Y. Savrasov, Electronic structure and magnetic properties of NaOsO_3 , *Phys. Rev. B* **85**, 174424 (2012).

- [4] M.-C. Jung, Y.-J. Song, K.-W. Lee, and W. E. Pickett, Structural and correlation effects in the itinerant insulating antiferromagnetic perovskite NaOsO_3 , *Phys. Rev. B* **87**, 115119 (2013).
- [5] I. L. Vecchio, A. Perucchi, P. Di Pietro, O. Limaj, U. Schade, Y. Sun, M. Arai, K. Yamaura, and S. Lupi, Infrared evidence of a Slater metal-insulator transition in NaOsO_3 , *Sci. Rep.* **3**, 2990 (2013).
- [6] S. Middey, S. Debnath, P. Mahadevan, and D. D. Sarma, NaOsO_3 : A high Neel temperature $5d$ oxide, *Phys. Rev. B* **89**, 134416 (2014).
- [7] S. Calder, J. H. Lee, M. B. Stone, M. D. Lumsden, J. C. Lang, M. Feyngenson, Z. Zhao, J.-Q. Yan, Y. G. Shi, Y. S. Sun, Y. Tsujimoto, K. Yamaura, and A. D. Christianson, Giant spin-

- phonon-electronic coupling in a $5d$ oxide, *Nat. Commun.* **6**, 8916 (2015).
- [8] B. Kim, P. Liu, Z. Ergönenc, A. Toschi, S. Khmelevskiy, and C. Franchini, Lifshitz transition driven by spin fluctuations and spin-orbit renormalization in NaOsO_3 , *Phys. Rev. B* **94**, 241113(R) (2016).
- [9] A. Sleight, J. Gillson, J. Weiher, and W. Bindloss, Semiconductor-metal transition in novel $\text{Cd}_2\text{Os}_2\text{O}_7$, *Solid State Commun.* **14**, 357 (1974).
- [10] D. Mandrus, J. R. Thompson, R. Gaal, L. Forro, J. C. Bryan, B. C. Chakoumakos, L. M. Woods, B. C. Sales, R. S. Fishman, and V. Keppens, Continuous metal-insulator transition in the pyrochlore $\text{Cd}_2\text{Os}_2\text{O}_7$, *Phys. Rev. B* **63**, 195104 (2001).
- [11] J. Yamaura, K. Ohgushi, H. Ohsumi, T. Hasegawa, I. Yamauchi, K. Sugimoto, S. Takeshita, A. Tokuda, M. Takata, M. Udagawa, M. Takigawa, H. Harima, T. Arima, and Z. Hiroi, Tetrahedral Magnetic Order and the Metal-Insulator Transition in the Pyrochlore Lattice of $\text{Cd}_2\text{Os}_2\text{O}_7$, *Phys. Rev. Lett.* **108**, 247205 (2012).
- [12] Z. Hiroi, J. Yamaura, T. Hirose, I. Nagashima, and Y. Okamoto, Lifshitz metal-insulator transition induced by the all-in/all-out magnetic order in the pyrochlore oxide $\text{Cd}_2\text{Os}_2\text{O}_7$, *APL Mater.* **3**, 041501 (2015).
- [13] W. J. Padilla, D. Mandrus, and D. N. Basov, Searching for the Slater transition in the pyrochlore $\text{Cd}_2\text{Os}_2\text{O}_7$ with infrared spectroscopy, *Phys. Rev. B* **66**, 035120 (2002).
- [14] C. H. Sohn, H. Jeong, H. Jin, S. Kim, L. J. Sandilands, H. J. Park, K. W. Kim, S. J. Moon, D.-Y. Cho, J. Yamaura, Z. Hiroi, and T. W. Noh, Optical Spectroscopic Studies of the Metal-Insulator Transition Driven by All-In-All-Out Magnetic Ordering in $5d$ Pyrochlore $\text{Cd}_2\text{Os}_2\text{O}_7$, *Phys. Rev. Lett.* **115**, 266402 (2015).
- [15] Whether this is representative of the bulk behavior or an effect limited close to the sample surface remains an open question.
- [16] H. Shinaoka, T. Miyake, and S. Ishibashi, Noncollinear Magnetism and Spin-Orbit Coupling in $5d$ Pyrochlore Oxide $\text{Cd}_2\text{Os}_2\text{O}_7$, *Phys. Rev. Lett.* **108**, 247204 (2012).
- [17] S. Calder, J. G. Vale, N. A. Bogdanov, X. Liu, C. Donnerer, M. H. Upton, D. Casa, A. H. Said, M. D. Lumsden, Z. Zhao, J. Q. Yan, D. Mandrus, S. Nishimoto, J. van den Brink, J. P. Hill, D. F. McMorrow, and A. D. Christianson, Spin-orbit-driven magnetic structure and excitation in the $5d$ pyrochlore $\text{Cd}_2\text{Os}_2\text{O}_7$, *Nat. Commun.* **7**, 11651 (2016).
- [18] C. Donnerer, M. C. Rahn, M. M. Sala, J. G. Vale, D. Pincini, J. Stremper, M. Krisch, D. Prabhakaran, A. T. Boothroyd, and D. F. McMorrow, All-in-all-Out Magnetic Order and Propagating Spin Waves in $\text{Sm}_2\text{Ir}_2\text{O}_7$, *Phys. Rev. Lett.* **117**, 037201 (2016).
- [19] H. Guo, C. Ritter, and A. C. Komarek, Direct determination of the spin structure of $\text{Nd}_2\text{Ir}_2\text{O}_7$ by means of neutron diffraction, *Phys. Rev. B* **94**, 161102(R) (2016).
- [20] Y. Wang, T. F. Rosenbaum, A. Palmer, Y. Ren, J.-W. Kim, D. Mandrus, and Y. Feng, Strongly-coupled quantum critical point in an all-in-all-out antiferromagnet, *Nat. Commun.* **9**, 2953 (2018).
- [21] N. A. Bogdanov, R. Maurice, I. Rousochatzakis, J. van den Brink, and L. Hozoi, Magnetic State of Pyrochlore $\text{Cd}_2\text{Os}_2\text{O}_7$ Emerging from Strong Competition of Ligand Distortions and Longer-Range Crystalline Anisotropy, *Phys. Rev. Lett.* **110**, 127206 (2013).
- [22] Note that the density of states is inequivalent to the RIXS cross section; the argument is that the single- and bimagnon processes should be dominant in the RIXS cross section.
- [23] T. M. H. Nguyen, L. J. Sandilands, C. Sohn, C. Kim, A. L. Wysocki, I.-S. Yang, S. Moon, J.-H. Ko, J. Yamaura, Z. Hiroi, and T. W. Noh, Two-magnon scattering in the $5d$ all-in-all-out pyrochlore magnet $\text{Cd}_2\text{Os}_2\text{O}_7$, *Nat. Commun.* **8**, 251 (2017).
- [24] M. M. Sala, K. Martel, C. Henriquet, A. A. Zein, L. Simonelli, C. Sahle, H. Gonzalez, M.-C. Lagier, C. Ponchut, S. Huotari, R. Verbeni, M. Krisch, and G. Monaco, A high-energy-resolution resonant inelastic X-ray scattering spectrometer at ID20 of the European Synchrotron Radiation Facility, *J. Synchrotron Radiat.* **25**, 580 (2018).
- [25] C. H. Sohn, C. H. Kim, L. J. Sandilands, N. T. M. Hien, S. Y. Kim, H. J. Park, K. W. Kim, S. J. Moon, J. Yamaura, Z. Hiroi, and T. W. Noh, Strong Spin-Phonon Coupling Mediated by Single Ion Anisotropy in the All-In-All-Out Pyrochlore Magnet $\text{Cd}_2\text{Os}_2\text{O}_7$, *Phys. Rev. Lett.* **118**, 117201 (2017).
- [26] S. Tóth and B. Lake, Linear spin wave theory for single-Q incommensurate magnetic structures, *J. Phys.: Condens. Matter* **27**, 166002 (2015).
- [27] We provide a natural explanation for this later in the paper.
- [28] The increase in width (and intensity) of the elastic line through the MIT is likely due to low-energy phonon excitations that cannot be discriminated due to the finite energy resolution.
- [29] J. G. Vale, S. Calder, C. Donnerer, D. Pincini, Y. G. Shi, Y. Tsujimoto, K. Yamaura, M. M. Sala, J. van den Brink, A. D. Christianson, and D. F. McMorrow, Evolution of the Magnetic Excitations in NaOsO_3 through its Metal-Insulator Transition, *Phys. Rev. Lett.* **120**, 227203 (2018); J. G. Vale, S. Calder, C. Donnerer, D. Pincini, Y. G. Shi, Y. Tsujimoto, K. Yamaura, M. Moretti Sala, J. van den Brink, A. D. Christianson, and D. F. McMorrow, Crossover from itinerant to localized magnetic excitations through the metal-insulator transition in NaOsO_3 , *Phys. Rev. B* **97**, 184429 (2018).
- [30] D. J. Singh, P. Blaha, K. Schwarz, and J. O. Sofo, Electronic structure of the pyrochlore metals $\text{Cd}_2\text{Os}_2\text{O}_7$ and $\text{Cd}_2\text{Re}_2\text{O}_7$, *Phys. Rev. B* **65**, 155109 (2002).
- [31] A. Irizawa, A. Higashiya, S. Kasai, T. Sasabayashi, A. Shigemoto, A. Sekiyama, S. Imada, S. Suga, H. Sakai, H. Ohno, M. Kato, K. Yoshimura, and H. Harima, Photoemission spectroscopy and X-ray absorption spectroscopy studies of the superconducting pyrochlore oxide $\text{Cd}_2\text{Re}_2\text{O}_7$, *J. Phys. Soc. Jpn.* **75**, 094701 (2006).
- [32] S. Gangopadhyay and W. E. Pickett, Spin-orbit coupling, strong correlation, and insulator-metal transitions: The $J_{\text{eff}} = \frac{3}{2}$ ferromagnetic Dirac-Mott insulator $\text{Ba}_2\text{NaOsO}_6$, *Phys. Rev. B* **91**, 045133 (2015).
- [33] A. E. Taylor, R. Morrow, R. S. Fishman, S. Calder, A. I. Kolesnikov, M. D. Lumsden, P. M. Woodward, and A. D. Christianson, Spin-orbit coupling controlled ground state in $\text{Sr}_2\text{ScOsO}_6$, *Phys. Rev. B* **93**, 220408(R) (2016).
- [34] L. Xu, N. A. Bogdanov, A. Princep, P. Fulde, J. Van Den Brink, and L. Hozoi, Covalency and vibronic couplings make a nonmagnetic $j = 3/2$ ion magnetic, *npj Quantum Mater.* **1**, 16029 (2016).
- [35] S. Calder, D. J. Singh, V. O. Garlea, M. D. Lumsden, Y. G. Shi, K. Yamaura, and A. D. Christianson, Interplay of spin-orbit

- coupling and hybridization in $\text{Ca}_3\text{LiOsO}_6$ and $\text{Ca}_3\text{LiRuO}_6$, *Phys. Rev. B* **96**, 184426 (2017).
- [36] A. E. Taylor, S. Calder, R. Morrow, H. L. Feng, M. H. Upton, M. D. Lumsden, K. Yamaura, P. M. Woodward, and A. D. Christianson, Spin-Orbit Coupling Controlled $J = 3/2$ Electronic Ground State in $5d^3$ Oxides, *Phys. Rev. Lett.* **118**, 207202 (2017).
- [37] H.-J. Werner, P. J. Knowles, G. Knizia, F. R. Manby, and M. Schütz, MOLPRO: A general-purpose quantum chemistry program package, *WIREs Comput. Mol. Sci.* **2**, 242 (2012).
- [38] D. Figgen, K. A. Peterson, M. Dolg, and H. Stoll, Energy-consistent pseudopotentials and correlation consistent basis sets for the $5d$ elements Hf–Pt, *J. Chem. Phys.* **130**, 164108 (2009).
- [39] F. Schautz, H.-J. Flad, and M. Dolg, Quantum Monte Carlo study of Be_2 and group 12 dimers M_2 ($\text{M} = \text{Zn}, \text{Cd}, \text{Hg}$), *Theor. Chem. Acc.* **99**, 231 (1998).
- [40] T. H. Dunning, Gaussian basis sets for use in correlated molecular calculations. I. The atoms boron through neon and hydrogen, *J. Chem. Phys.* **90**, 1007 (1989).
- [41] K. Pierloot, B. Dumez, P.-O. Widmark, and B. O. Roos, Density matrix averaged atomic natural orbital (ANO) basis sets for correlated molecular wave functions, *Theor. Chim. Acta* **90**, 87 (1995).
- [42] A. Berning, M. Schweizer, H.-J. Werner, P. J. Knowles, and P. Palmieri, Spin-orbit matrix elements for internally contracted multireference configuration interaction wavefunctions, *Mol. Phys.* **98**, 1823 (2000).